Measurement of the spin-excitation continuum in one-dimensional $KCuF_3$ using neutron scattering

D. Alan Tennant and Roger A. Cowley
Oxford Physics, Clarendon Laboratory, Oxford University, Parks Road, Oxford OX1 3PU, United Kingdom

Stephen E. Nagler
Department of Physics, University of Florida, Gainesville, Florida 32611

Alexei M. Tsvelik
Oxford Physics, Department of Theoretical Physics, Oxford University, Keble Road, Oxford OX1 3PU, United Kingdom
(Received 31 March 1995)

In this, and the following paper, we present the results of a detailed experimental investigation into the spin dynamics of the quasi-one-dimensional $S=\frac{1}{2}$ Heisenberg antiferromagnet $KCuF_3$. In this paper we report results of inelastic neutron-scattering measurements made using the MARI time-of-flight spectrometer at the Rutherford Appleton Laboratory. Measurement of the magnetic excitation spectrum was made in both the low-temperature phase, where the chains are ordered together, and in the high-temperature phase, where the correlations between chains become unimportant. We compare our measurements with the Müller ansatz, which is identified with a two-spinon cross section, and find excellent agreement with this. The effect of temperature on the excitation continuum was also investigated. A series of measurements were made at temperatures ranging from 20 to 200 K. These results are compared to the predictions of field theory for the one-dimensional Heisenberg chain. Again good agreement is found with the theoretical predictions. In the following paper measurements of the low-energy scattering in the ordered phase, made on a triple-axis spectrometer, are presented.

I. INTRODUCTION

The ground and excited states of the one-dimensional (1D) antiferromagnetic (AF) nearest-neighbor Heisenberg model (NNHM) is one of the classic problems in statistical mechanics and magnetism. The Hamiltonian for the 1D NNHM is given by

$$H=J\sum_i S_iS_{i+1} \tag{1}$$

where J is the magnetic exchange energy, which is positive for an antiferromagnet. The simple form of Eq. (1) belies the rich physical behavior that it displays, and an understanding of the physics of the AF NNHM in one dimension has proved a formidable task for theoretical and mathematical physicists over the last six decades. Two factors make this problem difficult: First, quantum fluctuations are at their strongest in one dimension and cannot be treated within a mean-field approach.[1] Second, nonlinear excitations play an important role in the dynamical behavior of one-dimensional systems.[2] The quite different low-lying excitation spectra of the integer and half-odd-integer AF NNHM's provides us with a dramatic illustration of the importance of these two factors.

Haldane[3] investigated the effects of exchange anisotropy and quantum fluctuations on the dynamics of Eq. (1). He did this by making use of a mapping onto the nonlinear σ model and found that the low-lying excitations of the integer and half-odd-integer AF NNHM were quite different. For integer chains he found that the excitations were spin waves, similar to the classical result, but with an energy gap in the dispersion arising from the zero-point fluctuations. The fluctuations create zero-energy solitons, which disorder the ground state and give rise to correlations that fall away exponentially with distance. However, when he tried using the same mapping for half-odd-integer chains, he found that an extra term entered the new Hamiltonian as a consequence of the Fermion nature of the spins. The extra term deconfines the $S=1$ spin of a spin wave into pairs of $S=\frac{1}{2}$ quantum solitons,[3] known as spinons. The pairs of spinons give a gapless continuum of excitations, and the ground state has correlations that decrease as a power law with distance.

Following Haldane's calculations, which were published in 1983, a great number of experimental and computational studies have been carried out.[4] Most of these have concentrated on the behavior of integer chains and have largely been confined to the case of the $S=1$ AF NNHM, where the effect is largest. This work has confirmed the behavior predicted by Haldane, and his conjecture is now widely accepted. Despite the extensive investigations of integer AF NNHM chains, little work has been undertaken on the $S=\frac{1}{2}$ AF NNHM, where quantum effects should be very visible as a continuum of excitations. We seek partially to redress this imbalance with our results published in this and the following paper.

We have already made[5] plused neutron-scattering measurements of the excitation spectrum of $KCuF_3$ prior to the ones reported here. This system is a good realization of an

0163-1829/95/52(18)/13368(13)/$06.00

$S=\frac{1}{2}$ AF NNHM,[6] and our results confirmed a continuum of magnetic excitations, as predicted. The extent and intensity of the continuum were consistent with the ansatz proposed by Müller *et al.*[7] However these measurements were not sufficiently detailed to allow a full quantitative comparison to be made with theory. In particular an accurate measurement of the nonmagnetic contribution was found to be crucial for determining the form of the broad components of magnetic scattering. In this and the following paper we report significantly more detailed measurements of the magnetic scattering in $KCuF_3$. These new measurements were made over a wide range of temperatures and study the continuum of excitations at high and low energies. In this paper, hereafter referred to as paper I, we confine ourselves to the measurements made using time-of-flight techniques. In the following paper, paper II, we present our measurements made in the ordered phase using a triple-axis neutron spectrometer.

In paper I we present the results of two neutron-scattering experiments on $KCuF_3$. Both of these were made using the multiangle rotor instrument (MARI), which is a time-of-flight spectrometer situated on the ISIS pulsed neutron source, Rutherford Appleton Laboratory, Didcot, England. Our first measurements were directed towards examining the effects of temperature, up to $T=200$ K, on the excitation continuum. Detailed field-theory calculations of the low-lying excited states are available in the literature,[8] and it was these that provided the impetus for this work. The calculations predict the variation in intensity and broadening of the scattering as a function of temperature, and our measurements aimed to test these predictions. The MARI instrument necessarily measures the scattering across a large swathe of energy and momentum transfer. Because of this, the measurements also provide information on the distribution of magnetic states of different energies over a large region of the Brillouin zone. The second set of measurements reported in this paper was concerned with measuring both the extent and strength of the quantum continuum below the 3D ordering temperature. The rest of this paper is organized as follows: Section II discusses the relevant theory. Section III describes the experimental procedures. Section IV presents the results of our measurements and analysis. The paper ends with a summary and conclusion in Sec. V. We leave a discussion of the results until the end of paper II.

II. THEORY

It is often possible to calculate a limited set of physical properties of 1D systems using exact methods. In 1931 Bethe[9] proposed an ansatz for the solution of the $S=\frac{1}{2}$ AF NNHM. Bethe's method allows calculation of a large number of physical properties, for example, the ground-state energy of the $S=\frac{1}{2}$ NNHM.[10] The dispersion of the lowest-lying excited states have been calculated by des Cloizeaux and Pearson[11] (dCP). The dCP dispersion is sinusoidal and is given by

$$\omega(Q_\parallel)=\pi J|\sin(Q_\parallel c)|, \tag{2}$$

where $Q_\parallel$ denotes the wave vector along the chain direction and c is the spacing between lattice sites. On reexamining dCP's calculation, Faddeev and Takhtajan[12] have proposed that the basic excitations that make up the continuum of excited states are pairs of $S=\frac{1}{2}$ "spinons," which they described as delocalized kinks; see also Fowler.[13] Each spinon has a wave vector restricted to only half of the Brillouin zone. Spinons are created and destroyed as pairs, and within this picture the dCP dispersion is understood to be a pair of spinons, one of which has zero energy.

Inelastic neutron-scattering experiments measure the magnetic response of the system as a function of energy and momentum transfer. The magnetic scattering cross section is proportional to the dynamical correlation function denoted by $S(\mathbf{Q},\omega)$. The components $S^{\alpha\beta}(\mathbf{Q},\omega)$ of this function are the Fourier transforms of the time-dependent two-spin correlation functions and are given by[14]

$$S^{\alpha\beta}(Q,\omega)=\frac{1}{2\pi\hbar N}\sum_{i,j}\exp[iQ\cdot(\mathbf{R}_j-\mathbf{R}_i)]\int_{-\infty}^{\infty}dt\,\exp(i\omega t)\times\langle S^{\alpha}{}_i(0)S^{\beta}{}_j(t)\rangle, \tag{3}$$

where $\mathbf{Q}$ is the wave-vector transfer from the scattered neutron to the system, ω is the energy transfer to the system by

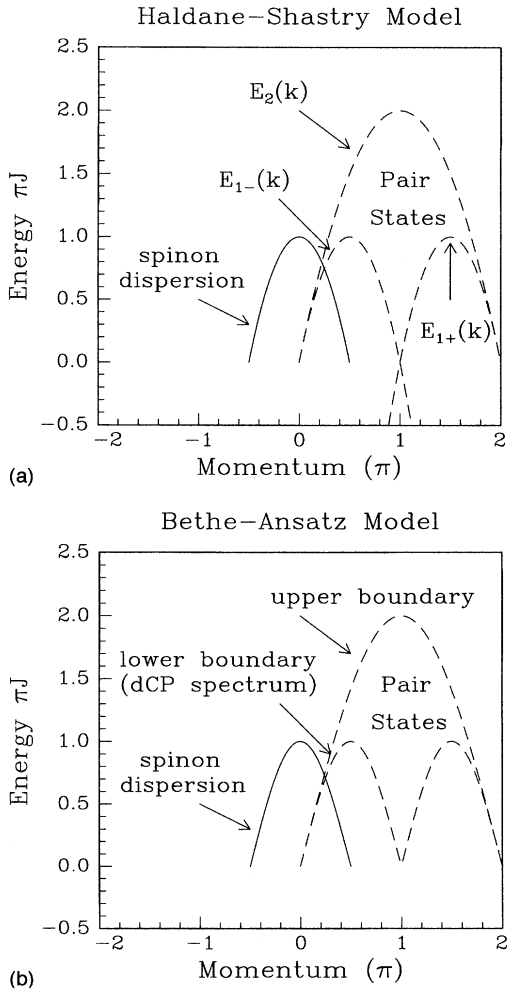

FIG. 1. (a) The spinon dispersion for the Haldane-Shastry model. The two spinon excitations form a continuum. (b) The excitation spectrum for the nearest-neighbor Heisenberg model as proposed by Müller.

the neutron, $\mathbf{R}_i$ and $\mathbf{R}_j$ are the positions of the ith and jth spins, respectively, N is the total number of spin sites, and α and β are Cartesian coordinates. Here the angular brackets denote a thermal average. Because the Hamiltonian in Eq. (1) commutes with the total z component of spin $S^z{}_T$, this implies that $S^{\alpha\beta}(\mathbf{Q},\omega)=0$ for $\alpha\neq\beta$.[14] Also, because the Hamiltonian is equivalent for all the spin directions x, y, and z, the nonzero components of $S(\mathbf{Q},\omega)$ are the same $S^{xx}=S^{yy}=S^{zz}$. Unfortunately Bethe's method is not amenable to calculating the dynamical correlation functions defined in Eq. (3), and therefore approximate methods have to be used.

By considering the available exact results, sum rules, and computer calculations Müller *et al.*[7] have constructed an ansatz, the Müller ansatz (MA), for the dynamical correlation functions of the 1D $S=\frac{1}{2}$ antiferromagnetic NNHM at $T=0$. Their expression is given by[7]

$$S^{\alpha\beta}(\mathbf{Q},\omega)=\frac{A}{2\pi}\,\delta_{\alpha,\beta}\frac{\Theta(\omega-\omega(Q_\parallel))\Theta(\omega^u(Q_\parallel)-\omega)}{\sqrt{\omega^2-[\omega^1(Q_\parallel)]^2}}. \tag{4}$$

where A is a constant [note that the factor of $1/(2\pi)$ is included in Eq. (4) because our defnition of $S(\mathbf{Q},\omega)$ given in Eq. (3) differs from that in Ref. 7], Θ is a Heaviside step function, which is defined as being zero when its argument is negative and equal to one otherwise, $\delta_{\alpha,\beta}$ is a Kronecker delta symbol, $\omega^1(Q_\parallel)$ is the dCP dispersion and constitutes the lower boundary of the continuum, and $\omega^u(Q_\parallel)$ is the expression for the upper boundary, which is given by

$$\omega^u(Q_\parallel)=2\pi J|\sin(Q_\parallel c/2)|. \tag{5}$$

Sum rules for the intensity can be obtained theoretically. The MA does not satisfy all the sum rules exactly and can only be an approximation to the real form of $S(\mathbf{Q},\omega)$. A multiplicative constant A is included in Eq. (4) to account for this. Using the sum rules derived by Hohenberg and Brinkmann,[15] Müller *et al.*, have calculated values of A in the range 1–1.5 depending on which sum rule they choose to satisfy.[7] One sum rule is that $S^{\alpha\alpha}(\mathbf{Q},\omega)$ integrated over $\mathbf{Q}$ and ω must be equal to the spin magnitude squared, $(S^z)^2=\frac{1}{4}$. This yields a value for A of 1.43.[7] The extent of the continuum of excited states proposed by Müller is shown in Fig. 1(b). Equation (4) predicts a square-root singularity at the lower boundary with an abrupt high-energy cutoff given by Eq. (5). Computer calculations[7] suggest that there is a small contribution of states with nonzero matrix elements outside the proposed continuum. However, these states have a scattering weight two orders of magnitude lower than the neighboring states, which lie within the boundaries. Recent numerical calculations[16] lend further support to the MA.

Recent theoretical advances have given a new interpretation to the MA as a two-spinon continuum. Haldane[17] and Shastry[18] have independently developed a new model for a 1D interacting Fermion system, which is related in a direct way to the NNHM. Their model is similar to the $S=\frac{1}{2}$ AF NNHM but with a coupling between spin sites, which decreases as $1/R^2$ with distance R. The Hamiltonian for the Haldane-Shastry model (HSM) is given by[17]

$$H=J\sum_{m<n}\frac{1}{[d(m-n)]^2}\,S_m\cdot S_n, \tag{6}$$

where $d(n)=(N/\pi)\sin(\pi n/N)\rightarrow n$ as the number of sites $N\rightarrow\infty$. The calculated spin correlations in the HSM take a particularly simple form: the solution by Haldane and Zirnbauer[19] shows this model to corresponds to an ideal spinon gas, in that the $S=\frac{1}{2}$ spinons are free. Each spinon has a quadratic dispersion relation[19]

$$\omega^{\rm sp}(Q_\parallel)=(J/2)[(\pi/2)^2-Q_\parallel^2], \tag{7}$$

and its wave vector is restricted to only half of the Brillouin zone, i.e., $|Q_\parallel|<\pi/2$. The dispersion of a spinon is shown in Fig. 1(a).

In the HSM the single-spin flip ($\Delta S=1$) excited state is expressible in terms of only two-spinon states, where the spins of each $S=\frac{1}{2}$ spinon are parallel.[19] The quantity $S(\mathbf{Q},\omega)$ in the limit of $T=0$, reflects this and is nonzero only at energies and wave vectors within the two-spinon continuum, also shown in Fig. 1(b). The dynamical correlation function $S(\mathbf{Q},\omega)$ at $T=0$ for the HSM model in terms of wave vector $Q_\parallel$ along the chain, and energy transfer ω is given by

$$S^{\alpha\beta}(\mathbf{Q},\omega)=\delta_{\alpha\beta}\frac{1}{2}\left[\frac{\Theta(\omega_2(Q_\parallel)-\omega)\Theta(\omega-\omega_{1-}(Q_\parallel))\Theta(\omega-\omega_{1+}(Q_\parallel))}{\sqrt{[\omega-\omega_{1-}(Q_\parallel)][\omega-\omega_{1+}(Q_\parallel)]}}\right], \tag{8}$$

where the dispersion relations ω_{1-}, ω_{1+}, and ω_2 are given by the equations[19]

$$\begin{aligned}\omega_{1-}(Q_\parallel)&=(J/2)Q_\parallel(\pi-Q_\parallel),\\ \omega_{1+}(Q_\parallel)&=(J/2)(Q_\parallel-\pi)(2\pi-Q_\parallel),\\ \omega_2(Q_\parallel)&=(J/4)Q_\parallel(2\pi-Q_\parallel),\end{aligned} \tag{9}$$

where the subscripts $1-$ and $1+$ denote one-spinon dispersion relations, these constitute a lower two-spinon boundary. The dynamical correlations exhibit a square-root singularity at the lower boundary and are confined within the two-spinon continuum of states as shown in Fig. 1(b).

Haldane and Zirnbauer[19] have pointed out the similarity of Eq. (8) to the MA, Eq. (4). Indeed if the quadratic dispersion of Eq. (7) is replaced by a sinusoidal dispersion $\omega^{\rm sp}=\pi J\cos(Q_\parallel c)$ then this yields a lower two-spinon boundary given by the dCP dispersion, Eq. (2), and an upper two-spinon boundary identical to $\omega^u(Q_\parallel)$, Eq. (5). Substituting $\omega_{1-}(Q_\parallel)=\pi J\sin(Q_\parallel c)$, and $\omega_{1+}(Q_\parallel)=-\pi J\sin(Q_\parallel c)$ into Eq. (8) gives the MA, Eq. (4). This identifies the MA

with the two-spinon cross section of the 1D AF NNHM.[19,20] Within this picture the small contributions outside the continuum are identified with processes in which more than two spinons are created.

Field theory gives a framework within which to calculate physical quantities of direct experimental interest.[21] Such calculations are really only valid in the low-energy and long-wavelength limit but nevertheless provide a more general approach to problems than highly specific techniques, such as the Bethe ansatz. Using field theory, Schulz[8] has calculated the temperature-dependent correlation functions for the 1D $S=\frac{1}{2}$ AF NNHM. The Green's functions for the components of spin S^{α} and S^{β} are defined as

$$G^{\alpha\beta}(x,t)=-i\Theta(t)\langle[S^{\alpha}(x,t)S^{\beta}(0,0)]\rangle,$$

$$G^{\alpha\beta}(Q,\omega)=-\int\int_{-\infty}^{\infty}dx\,dt\,e^{i(\omega t-qx)}\Theta(t) \qquad (10)$$

$$\times\langle[S^{\alpha}(x,t),S^{\beta}(0,0)]\rangle.$$

For wave vectors close to the antiferromagnetic point, $Q_{\parallel}\approx\pi/c$, the form of $G^{\alpha\beta}(Q,\omega)$ is given by[8]

$$G^{\alpha\beta}(\mathbf{Q},\omega)=\frac{1}{4}\left(\frac{A}{2\pi}\right)\delta_{\alpha,\beta}(n_{\omega}+1)\frac{1}{T}$$

$$\times\rho\left(\frac{\omega-vq}{4\pi K_B T}\right)\rho\left(\frac{\omega+vq}{4\pi K_B T}\right), \qquad (11)$$

where

$$\rho(x)=\frac{\Gamma(\eta-ix)}{\Gamma(1-\eta-ix)} \qquad (12)$$

and Γ is a complex gamma function. In the expression $q=Q_{\parallel}-\pi$, $Q_{\parallel}$ is the component of $\mathbf{Q}$ along the chain direction and $v=\pi J$; the continuum approximation of a linear dispersion relation ($\omega=vq$) has been made. The exponent $\eta=\frac{1}{4}$ is the value for the discrete lattice.[22] The multiplicative factors make the scattering in Eq. (11) consistent with the MA, where A is the same constant defined in Eq. (4).

The dynamical scattering function $S(\mathbf{Q},\omega)$ can be easily written in terms of the Green's function,

$$S^{\alpha\beta}(\mathbf{Q},\omega)=-\frac{i}{\pi\hbar}(n_{\omega}+1)\mathscr{I}[G^{\alpha\beta}(\mathbf{Q},\omega)] \qquad (13)$$

where $\mathscr{I}$ denotes the imaginary part, and for $T=0$ this has a square-root singularity at the lower boundary in agreement with Eqs. (4) and (8). As the temperature increases the scattering cross section broadens and scattering weight moves to higher energies. Further details of the correlation functions for the $S=\frac{1}{2}$ NNHM are given in an appendix at the end of this paper. This includes a calculation of the extension of the correlation functions to include higher-order operators. Consideration of these higher-order terms are important at high energies; see Sec. IV C.

III. EXPERIMENTAL METHOD

$KCuF_3$ is a good example of a quasi-one-dimensional Heisenberg antiferromagnet.[6] It is nearly tetragonal, with low-temperature lattice parameters of $a=b=4.126$ Å, and $c=3.914$ Å.[23] The 1D properties are the result of a Jahn-Teller distortion, which displaces the fluorines in the a-b plane away from the midpoint of the Cu^{2+}—Cu^{2+} bonds.[6] Two possible polytypes result, which are denoted by (a) and (d), corresponding to different ordering of the fluorines between layers. The two structures are shown in Fig. 2. Quenching of the orbital angular momentum by the crystal field results in a spin-only moment of $S=\frac{1}{2}$ for each Cu^{2+} ion. The unpaired electron in the Cu^{2+} ion is in a $d_{x^2-y^2}$ orbital, which is oriented such that significant overlap with the F^- ions occurs only along the c axis. Strong antiferromagnetic exchange results along the c direction, with much weaker ferromagnetic exchange along the a and b directions. At low temperatures the ferromagnetic exchange between the magnetic c-axis chains results in long-range ordering. The Néel ordering temperature differs for the two polytypes; $T_N=39$ K for type (a) and $T_N=22$ K for type (d).[23] A small xy anisotropy confines the spins to lie in the a-b plane at low temperatures.[23]

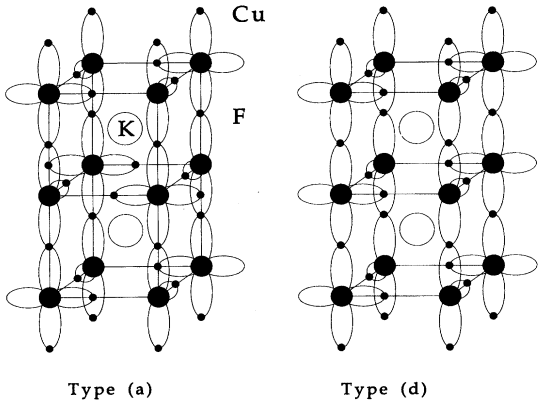

FIG. 2. The crystal structure of $KCuF_3$. The two polytype structures (a) and (d) are shown. These are distinguished by the different displacements of fluorine ions in the a-b plane.

Inelastic neutron-scattering measurements were made on the large single-crystal (6.86 g) of $KCuF_3$ consisting of 99% of polytype (a) ($T_n=39$ K) used for earlier measurements of the excitations. The MARI time-of-flight chopper spectrometer was used, and the measurements were made in two stages separated by several months with the same experimental setup and method being employed for both stages. The sample was mounted within an aluminum can containing He contact gas and fixed on the instrument goniometer with the a and c axes horizontal. A closed-cycle refrigerator was used to cool the crystal down to $T=20$ K and gave temperature control to an accuracy of ±0.1 K over several days.

The MARI spectrometer works as follows:[24] A high-intensity pulse of neutrons is produced by spallation every 20 mS. The neutrons are moderated to useful energies by a methane moderator and monochromated by a fast Fermi chopper. This produces a monochromatic beam of energy E_0, variable between 10 and 2000 meV, with an intrinsic energy resolution of approximately 2% full width at half maximum of the incident energy E_0. A slow chopper reduces the fast-neutron background. The scattered neutrons are measured in an array of high-pressure ^{3}He detectors. The

detectors are located a distance of 4.022 m away from the sample position. A low-angle array of 109 detectors are arranged symmetrically around the incident neutron direction into eight banks covering scattering angles from 3.86° to 12.0°. High-angle detector banks measure the scattering at larger momentum transfers and extend over scattering angles from 12° to 135°. From the time of detection of a scattered neutron in a particular detector, both the energy (E_T) and momentum ($\mathbf{Q}$) transfer to the sample are calculated.[24]

Scans on time-of-flight instruments are constrained by the conservation of momentum and energy to measure momentum and energy transfers, which lie along a well-defined locus. For an incident neutron of wave vector $\mathbf{k}_i$, and energy E_i, which is scattered into a detector at a scattering angle ϕ with final wave vector $\mathbf{k}_f$, and energy E_f we define a wave-vector transfer to the sample $\mathbf{Q}=\mathbf{k}_i-\mathbf{k}_f$, and an energy transfer to the sample $E_T=E_i-E_f$. The wave-vector transfer $\mathbf{Q}$ can then be split into a component $\mathbf{Q}_\parallel$ directed along the incident neutron axis and a component $Q_\perp$ perpendicular to the incident neutron axis: $\mathbf{Q}=\mathbf{Q}_\parallel+\mathbf{Q}_\perp$. The magnitude of these components is

$$Q_\parallel(E_i,\phi,E_T)=k_i-k_f\cos(\phi)$$
$$=\sqrt{E_i/\gamma}-\sqrt{E_i-E_T/\gamma}\,\cos(\phi), \quad (14)$$
$$Q_\perp(E_i,\phi,E_T)=k_f\sin(\phi)=\sqrt{E_i-E_T/\gamma}\,\sin(\phi)$$

in terms of the incident energy E_i, scattering angle ϕ, and energy transfer E_T. The kinematical constant $\gamma=2.072$ Å^2 meV. The energy transfer has a quadratic type of dependence on the momentum transfer. This is illustrated in Fig. 3(a), where a trajectory in $Q_\parallel$ and E_T is shown for a detector at $\phi=8°$ for $E_i=148.9$ meV. This is overlaid on the predicted continuum, Eq. (4). By changing the incident energy and scattering angle, measurements along different slices of $Q_\parallel$ and E_T can be made.

With the crystal mounted on the MARI spectrometer in the manner described above, it was then cooled below the Néel temperature $T_N=39$ K. The appearance of the $(0,0,\frac{1}{2})$ magnetic Bragg peak at $T=39$ K confirmed the ordering of the magnetic moments. A series of measurements with incident neutron wave vector $\mathbf{k}_I$ parallel to the chain direction, i.e., $\mathbf{k}_i\|(0,0,l)$ and perpendicular to the chain direction, $\mathbf{k}_i\|(h,0,0)$, were made at temperatures of 20, 50, 100, 150, and 200 K. An incident neutron energy of $E_0=148.9$ meV was used in all of these measurements. The scattering trajectory into a detector at $\varphi=8°$ is shown in Fig. 3(a). Each measurement was made with a total integrated intensity of 1500 μA h ($\sim$12 h). Measurements of the scattering from a standard V sample in a white beam was made before and after the experiment. In addition, measurements of the scattering from the V standard were made using a monochromated $E_0=148.9$ meV beam of neutrons. These were used to identify faulty detectors and calculate the absolute scattering cross section.

In the second part of the experiment the magnetic response in the 3D ordered phaes was probed in more detail. Measurements were made with incident energies of $E_0=127$, 140, 180, and 280 meV. During this second set of measurements problems in the seal protecting the instrumental vacuum led to water condensing on the experimental chamber. This gave rise to a small amount of ice accumulating on the sample. At low pressures and temperatures H_2O freezes into the Ih ice structure,[25] and scattering from vibrational and librational modes of this structure were observed.

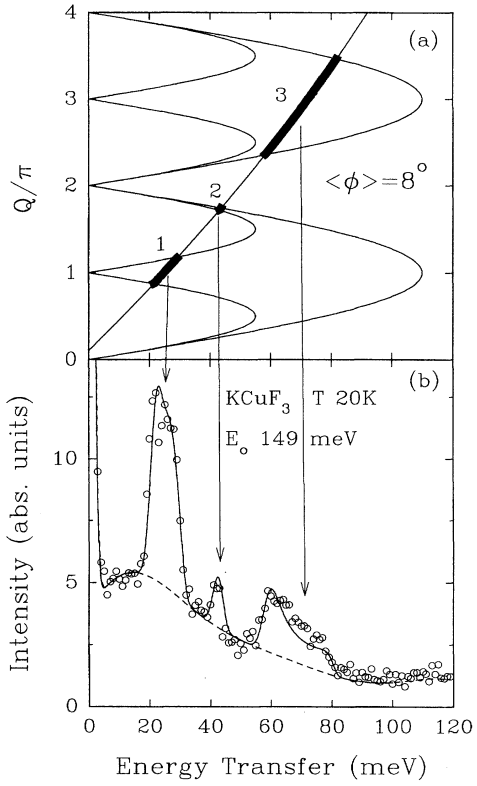

FIG. 3. (a) Scattering trajectory for a detector at a scattering angle of 8° and an incident energy of $E_0=148.9$ meV for $\mathbf{k}_i$ along c^* in $KCuF_3$. Scattering results when the trajectory intersects with the continuum (bold line). (b) Scattering measured in the low-angle detector banks at $T=20$ K. The solid line is a fit, as discussed in the text.

IV. RESULTS AND ANALYSIS

In this section, the results of our measurements are presented. For convenience we have split the results into two parts. In the first part, those measurements made below the Néel ordering temperature are considered. Comparison is made with the MA. Absolute cross sections and exchange parameters are obtained. In the second part, the scattering at higher temperatures is examined. These results are compared with the MA and field theory.

A. Absolute scattering cross sections

Comparison of scattering measurements to that from a V standard sample allows the normalization of total cross sections measured on the MARI spectrometer. The total incoherent scattering from the V standard at each incident energy was used to determine the absolute cross section. Corrections were made for the relative number of scattering centers in the $KCuF_3$ sample and V standard and the resultant absolute

cross section expressed in standard units. In the case of $KCuF_3$ this is a mb/meV/sr/Cu^{2+} atom.

The inelatsic neutron-scattering cross section per magnetic ion is given by[14]

$$\frac{d^2\sigma}{d\Omega\, dE'} = N\sigma_{\rm mag}\sum_{\alpha\beta}\frac{k'}{k}\left(\frac{g}{2}\right)^2 |F(\mathbf{Q})|^2(\delta_{\alpha\beta}-\tilde{\kappa}_\alpha\tilde{\kappa}_\beta) \times(n_\omega+1)S^{\alpha\beta}(\mathbf{Q},\omega), \quad (15)$$

where N is the number of scattering centers, the constant $\sigma_{\rm mag}=0.2896$ b, $\delta_{\alpha,\beta}$ is a Kronecker delta function, and the product of the components of the unit scattering vector along the directions α and β are subtracted from $\delta_{\alpha,\beta}$, g is the Landé g factor, which has been determined for $KCuF_3$ using electron spin resonance (ESR) and magnetic susceptibility techniques,[6] and F is the magnetic form factor for the Cu^{2+} ion.[26] Because the g factor for the magnetic d orbital is anisotropic, an average value $\langle g^2\rangle$ is used. Using numerical values for these, the factor A in the MA, Eq. (4) can be extracted from fits to the normalized experimental data.

B. Measurements below T_N

Figure 3(b) shows data measured in the low-angle detector banks (scattering angles $\phi=3.86°-12°$), at a temperature of $T=20$ K (well below the 3D ordering temperature), where the sample has been aligned with the c axis along the incident neutron wave vector $\mathbf{k}_i$. Scattering into detectors at higher angles was not considered as the strong wave-vector transfer dependence of the multiphonon scattering gave rise to a large nonmagnetic signal. All data have been correctly normalized to the scattering from a standard mass of V. The units of the corrected data are in mb/meV/sr/Cu^{2+}. A comparison of the eight radial banks showed that the scattering into each was identical (within the statistical uncertainties) and could be summed together without loss of information. Multiphonon processes contribute a smoothly varying signal underlying the magnetic scattering.

Measurement of the nonmagnetic scattering from the empty can alone suggests that this accounted for only $\sim 20\%$ of the total nonmagnetic contribution. In this case it became necessary to determine the scattering from the sample and mounting together. This was done by rotating the sample by 90° and measuring the nonmagnetic contribution in the vertical detector banks.[5] The 1D Heisenberg antiferromagnet has vanishing intensity as $Q_\parallel\rightarrow 0$. When the crystal is oriented such that the chain axis is perpendicular to the incoming beam, the neutrons scattered into the vertical detector banks have only a small wave-vector transfer along the chain direction. Therefore, the magnetic contribution is expected to be small. Since the crystal is nearly cubic, the nonmagnetic scattering should not be significantly different, and this gives a direct measure of the nonmagnetic scattering.

Figure 4 shows the measured nonmagnetic background. The solid line is a model of the nonmagnetic scattering: A Gaussian is used for the quasielastic peak and a polynomial for the smoothly decreasing component. The detectors in the vertical bank are 30 cm wide, and, as they are a distance of 4.022 m away from the scattering center, they subtend a small angle along the chain direction. The small component

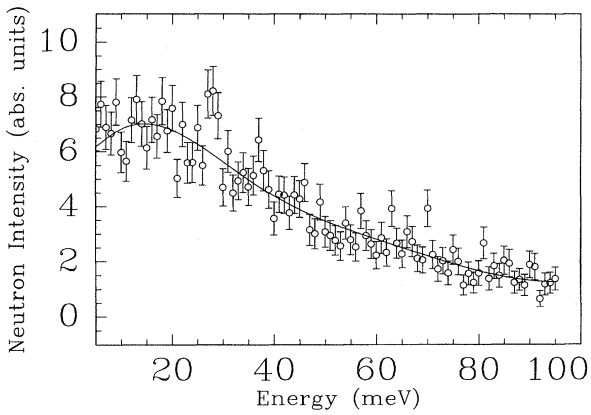

FIG. 4. Nonmagnetic background measured in the vertical low-angle banks at $T=20$ K for an incident energy of 148.9 meV, the 1D c axis was perpendicular to $\mathbf{k}_i$.

of wave-vector transfer directed along the chain contributes a small amount of magnetic scattering. A calculation of this magnetic scattering based on the MA reveals that this contribution is small enough to be ignored.

The solid line shown in Fig. 3(b) is the result of a least-squares fit of the background component and MA convolved with the instrumental resolution, as described in Ref. 5. The only parameters allowed to vary in this fit were the overall amplitude factor A, as defined in Eq. (4), the exchange interaction J, and a coefficient β, which scales the smooth nonmagnetic background determined using the method described above. This additional factor β should ideally be unity but has been allowed to vary in order to account for factors such as self-absorption of the crystal and the small detector-width effect. The constant β determined in this way is consistently in the range of values $\beta=0.85\pm0.05$ for *all* fits described here. For example, the background shown in Fig. 3(b) is scaled by a factor $\beta=0.870$.

Calculation of the measured cross section for a particular model is prohibitively slow to allow least-squares fitting of the exchange constant J. A number of scans were calculated for different values of J. Using an interpolation method, an exchange energy $\pi J=53.5\pm1.0$ meV was found to give the best fit. We have expressed the fitted value as πJ, the zone-boundary energy of the lower boundary, as this avoids confusion over renormalization factors between fits to classical models, as in Ref. 23, and the dCP dispersion, Eq. (2). This value is seen to give an excellent description of the data, Fig. 3(b). When correctly normalized to the V standard, fitting to the overall amplitude allows a determination of the multiplicative constant A in Eq. (5). The best fit value at $T=20$ K is $A=1.78\pm0.01\pm0.5$, for an exchange of $\pi J=53.5$ meV. The first error in A represents that of a fit to the model. The uncertainty in the value is dominated by the second error, which represents an estimated 30% uncertainty in the normalization procedure itself. The origin of this uncertainty is largely due to the uneven flux distribution across the incident beam. The fitted value of A is in agreement with the theoretical value $A\sim1.43$ calculated using sum rules.[7] As an additional check on the fitting method, the constants of the polynomial background were also allowed to vary. This gave no significant improvement in the goodness of fit.

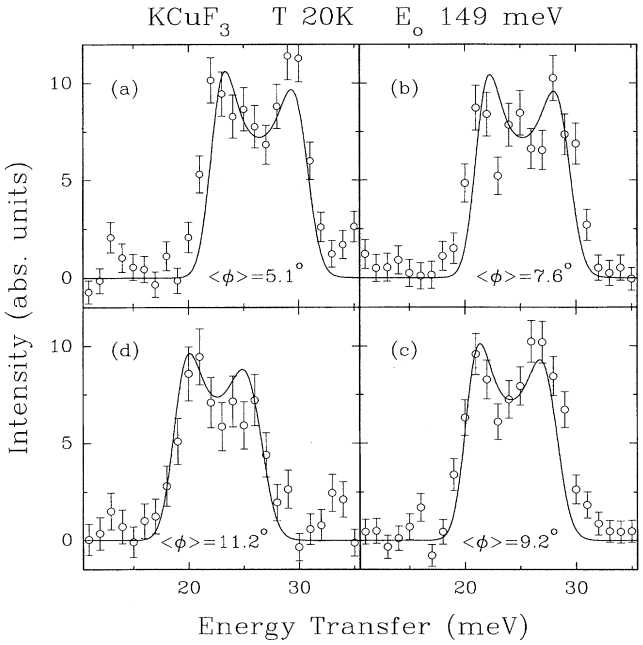

FIG. 5. Magnetic scattering with $\mathbf{k}_i$ directed along c^* measured at $T=20$ K for concentric rings of detectors corresponding to different scattering angles as discussed in the text. The weighted average scattering angle is indicated in each case. The low-energy field theory of Schultz is shown by solid lines (see text).

It is convenient for the purposes of discussion to divide the magnetic scattering into the three regions marked on Fig. 3. Region 1 is the low-energy scattering around the antiferromagnetic point $Q_\parallel=\pi/c$. The energy transfers involved, about 25 meV, are well below the zone-boundary energy, $\pi J=53.5$ meV. In this region the field-theory continuum result for the antiferromagnetic correlations, Eq. (11), is applicable. Region 2 shows a sharp feature at $\omega\approx 42$ meV arising from the ferromagnetic branch close to $Q_\parallel=2\pi/c$. At this energy one would expect higher-order terms in the field theory to become important [Eq. (A8) in the Appendix]. Finally, region 3 corresponds to magnetic scattering in the second Brillouin zone. The energy transfers are above the zone-

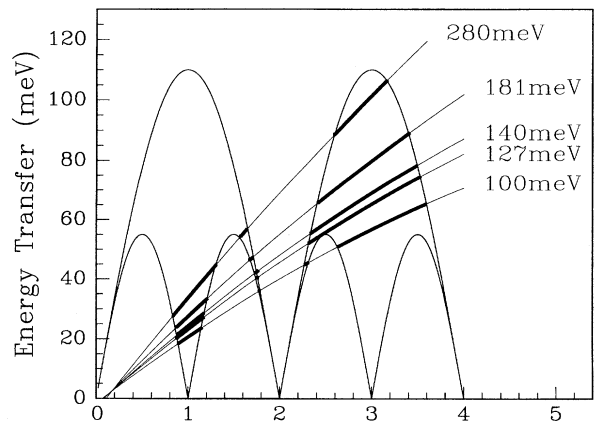

FIG. 6. Scattering trajectories projected onto the c axis for a number of incident energies.

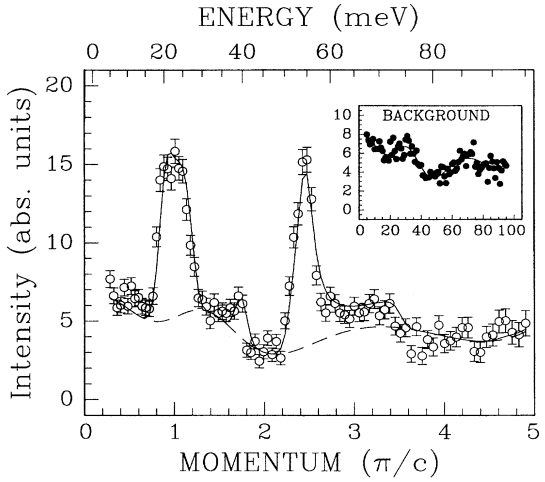

FIG. 7. Scattering measured in the low-angle banks at $T=20$ K for an incident energy of 127 meV. The solid line is the scattering calculated using the Müller ansatz added onto a fitted background as described in the text. The background is shown in the inset.

boundary energy and will henceforth be referred to as "the high-energy response." The field method is not applicable at these energy transfers, and the only variable model of the scattering in this region is the MA, Eq. (4).

The resolution of the scattering at low-energy transfers can be improved if the data are further divided into smaller ranges of scattering angles, thereby giving increased wave-vector resolution. Figure 5 shows scattering recorded at a temperature of $T=20$ K. Only the scattering in region 1 has been shown. The data have been divided into concentric rings of detectors with the following values of scattering angle ϕ: (a) 3.86°–6.43°, (b) 6.86°–8.14°, (c) 8.57°–9.86°, and (d) 10.29°–12°. The data have been normalized using the same procedure as that outlined for Fig. 3(b). In addition, a smooth functional form for the nonmagnetic background was determined as above, and this was subtracted to leave only magnetic scattering. The extra wave-vector resolution achieved by subdivision is apparent when one contrasts Figs. 3(b) and 5. The solid lines in Fig. 5 are the scattering profiles calculated for each ring using the low-energy field theory for $T=20$ K. This calculation includes resolution and form factor effects, as described in 5 and uses the parameters determined in the fit shown in Fig. 3(b). It is evident from this figure that the calculation provides an excellent description of the observed scattering. Although strictly a 1D theory, which ignores the effects of interchain coupling, the field-theory calculation reproduces the position, line shape, and intensity of the $Q_\parallel\sim\pi/c$ scattering correctly.

The energy and wave-vector dependence of the quasi-1D magnetic response at $T=20$ K in the 3D ordered phase was investigated more fully in a second series of measurements made using the following incident energies: 127, 140, 181, and 280 meV. The scattering trajectories for a detector at a scattering angle of $\phi=8°$ and these incident energies are shown in Fig. 6. A small amount of ice in the sample chamber complicated the background subtraction slightly, but the method of analysis remains essentially the same as that described above.

Figure 7 shows the data measured when **c** was aligned along $\mathbf{k}_i$ at $T=20$ K for an incident neutron energy of $E_0=127$ meV. The data is a summation over the scattering into the low-angle banks. The uppermost of the two vertical detector banks has been excluded from this summation as the scattering in this bank showed an anomalous incoherent component. Comparison of the scattering in each of the remaining banks confirmed that the scattering into each one of these was identical within the statistical accuracy. In Fig. 7 strong magnetic scattering is again clearly distinguishable from the multiphonon background. The scattering measured in the low-angle detector banks where **c** was aligned perpendicular to $\mathbf{k}_i$ is shown in the inset of Fig. 7. The upper detector bank is again excluded from this summation. There are insufficient counts in the remaining lower vertical bank for the background to be determined reliably from this alone. A comparison was made between the remaining banks and the scattering into each of these were found to be indistinguishable from the others. Assuming that any quasi-1D magnetic contribution is small, the nonmagnetic cross section was determined from the scattering by summing over the remaining seven banks.

The nonmagnetic scattering in Fig. 7 was modeled as before, by using a Gaussian quasielastic peak and polynomial, to which two more Gaussians were added. The two additional Gaussians in this model have been included to account for the dispersionless vibrational mode at 35 meV and the broad librational mode of ice Ih, which extends from 70 to 110 meV.[25] Both modes were clearly visible in the high-angle detector banks, confirming their nonmagnetic origin. The dashed line shown in the inset of Fig. 7 is a best fit of this functional form to the measured nonmagnetic background. This form gives an excellent description of the background scattering.

The solid line shown in Fig. 7 is the result of a best fit using the MA form of the scattering cross section, this being the only form of $S(\mathbf{Q},\omega)$ that is defined over the entire scattering range. Again the amplitude, exchange constant, and scaling factor β multiplying the background were determined from the fit. The background scaling factor $\beta=0.865\pm0.005$ and this gives the nonmagnetic component shown in the figure as a dashed line. As the scattering trajectories pass close to the singularity at the zone boundary, strong scattering is observed at about 55 meV. The intensity of this peak is strongly coupled to the exchange constant. Determining this by interpolation yields an improved zone-boundary energy of $\pi J=54.5\pm0.3$ meV. The amplitude A was found to be $1.81\pm0.01\pm0.5$.

1. Magnetic response at low energies in the ordered phase

Other incident neutron energies were used to probe the magnetic response at $T=20$ K. Figures 8 and 9 show scans taken using $E_0=140$ and 180 meV, respectively, and are summations over the low-angle detector banks. The normalized data measured with $E_0=140$ and 180 meV belong to the second stage of this experiment. The backgrounds for each have been independently determined, as before. Figures 8 and 9 show the scattering calculated using the MA and exchange and amplitude factors determined in the fit to the $E_0=127$-meV data, Fig. 7. Once again these parameters provide a good description of the data.

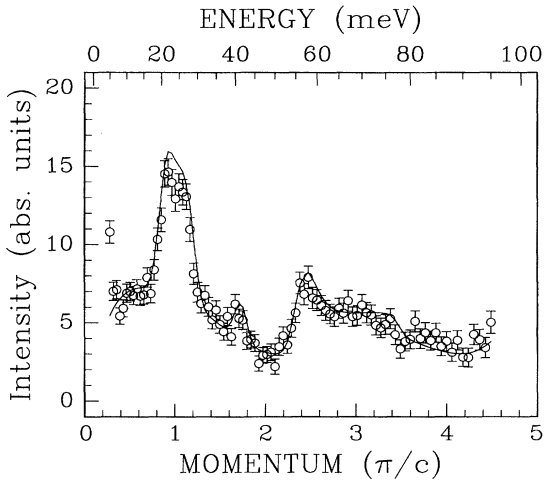

FIG. 8. Scattering measured in the low-angle banks at $T=20$ K for an incident energy of 140 meV. The solid line is the scattering calculated using the Müller ansatz added onto a fitted background, as described in the text.

Subdivision of the low-angle banks into rings has been shown to give increased wave-vector resolution at low energies. With the data accumulated at different energies, the low-energy scattering can be looked at in more detail. Figure 10 shows the scattering loci of a number of incident energies and for the particular rings of detectors at $T=20$ K. The scattering into rings of detectors for these incident energies are shown in Figs. 11(a), 11(b), 12(a) and 12(c). The measured scattering profiles are shown as a function of momentum transfer along $\mathbf{c}, Q_{\|}$. The corresponding energy transfers are shown on top of each graph as a nonlinear scale. The axes of these graphs have been restricted to **Q** transfers in the first Brillouin zone, i.e., low energies.

The solid lines are calculations using no adjustable parameters, as described already. This calculation reproduces the intensity, profile, and variation in energy of the con-

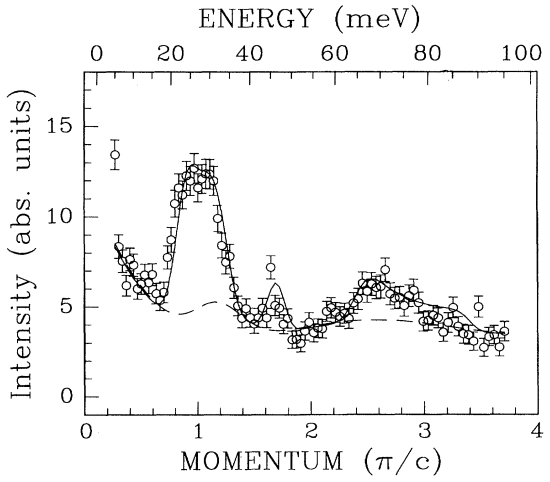

FIG. 9. Scattering measured in the low-angle banks at $T=20$ K using an incident energy of 180 meV. The solid line is the scattering calculated using the Müller ansatz added onto a fitted background as described in the text.

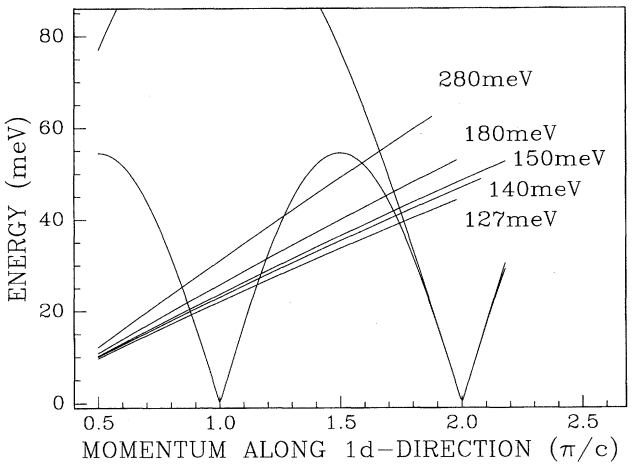

FIG. 10. Loci of scattering into detector rings at various energies. These loci correspond to those scans depicted in Figs. 11 and 12.

tinuum scattering. The Müller ansatz provides an impressively good description of the data in regions 1 and 2, the low-energy response.

2. *Magnetic response at high energies in the ordered phase*

The incident energies were chosen so as to allow the response in the neighborhood of the lower-boundary frequency to be investigated in more detail. These were selected so as to build up a cross section of the scattering around the zone-boundary frequency of the lower boundary at a wave vector $Q_{\parallel}=5\pi/2c$. Figure 6 shows the scattering trajectories for a detector at $\phi=8°$. In particular, the incident energy of $E_0=127$ meV was chosen because it bisects the antiferromagnetic zone boundary. (AFZB) at this point. Other incident energies give different scattering frequencies for the same wave vector. For an incident energy of 100 meV the

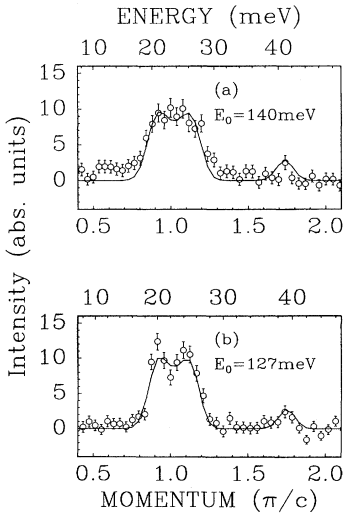

FIG. 11. Scans into ring (c), i.e., scattering angles φ from 8.57° to 9.86° at 20 K for (a) $E_0=140$ meV, and (b) $E_0=127$ MeV. The solid lines are calculated using the Müller ansatz as described in the text.

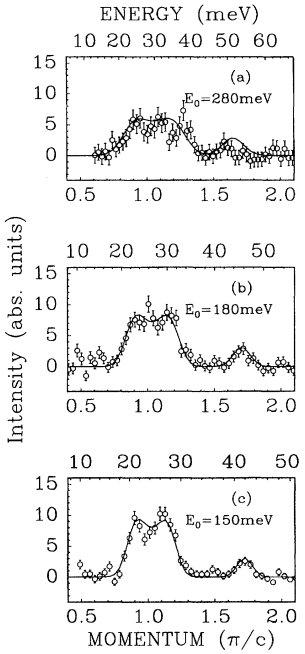

FIG. 12. Scattering measured at $T=20$ K for (a) $E_0=280$ meV, $\varphi=10.29°-12°$, (b) $E_0=180$ meV, and (c) $E_0=150$ meV for $\varphi=8.57°-9.86°$. The solid lines are calculated using the Müller ansatz, as described in the text.

scattering trajectory passes well below the AFZB frequency. In contrast, incident energies of $E_0=140$ and 181 meV pass above this zone-boundary energy. Subdivision into rings for each incident energy gives considerably better resolution and the response can be more thoroughly investigated close to the boundary. Figures 13(a)–13(d) shows some of the measured scattering profiles as a function of wave-vector transfer. Figure 13(a) shows a measurement for $E_0=100$ meV and displays a dip in intensity for $Q_{\parallel}=5\pi/2c$. Note that this scan was made at $T=50$ K, above the Néel ordering temperature. This is consistent with the scattering trajectory passing below the AFZB frequency, and because of this it necessarily intersects the lower boundary twice producing the peaked structure. Figures 13(b)–13(d) indicate that scattering decreases strongly from the maximum as the incident energy is increased. This is as expected. The solid lines are the calculations of the scattering using the same values of the exchange and overall amplitude parameters. The background parameter β was allowed to vary in subtracting the nonmagnetic scattering in order to reflect small differences in the nonmagnetic scattering as a function of angle. However, the fitted values of β were all within a few percent of each other, reflecting the soundness of method.

C. Measurements above T_N

Measurement of the scattering cross section was also made at temperatures above the 3D ordering temperature. Figure 14(a) shows the scattering measured in the low-angle banks at $T=50$ K. A smooth nonmagnetic background has been scaled and subtracted. Figure 14(b) shows the scattering at 20 K with the background subtracted. The solid line in both figures are calculations using the MA with the param-

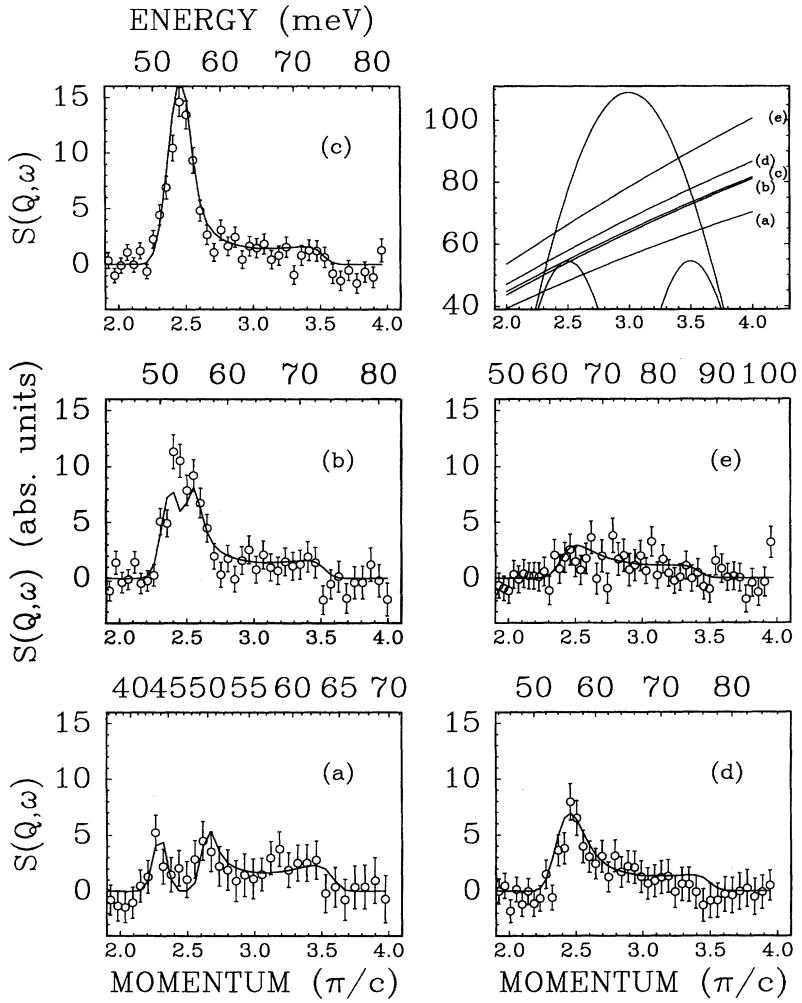

FIG. 13. Scans measuring the high-energy response at $T=50$ K, resolved into rings and made at different E_0. Each scan trajectory is shown in the top right-hand box. The solid lines are calculated using the Müller ansatz, as described in the text.

eters A and J determined in Fig. 3(b). These two plots show that the scattering profile is not changed on going above the Néel temperature.

Figure 15 shows the effects of temperature on region 1, up to $T=200$ K. To obtain adequate statistics at higher temperatures (100–200 K) the scattering is a summation over the entire low-angle detector banks. The data have been correctly normalized, and the nonmagnetic backgrounds, independently determined for each temperature, have been subtracted. The scattering broadens and weakens with increasing temperature. The solid line is that calculated using the low-energy field theory, with an exchange J and overall amplitude A fixed to the low temperature fits. The theoretical expression does not account for the small peak at about 42 meV. Aside from that, the agreement with experiment is excellent over the entire temperature range.

Figure 16 shows the scattering measured in region 2. This scattering is from the branch arising from the $Q_{\parallel}=2\pi/c$ nuclear point, and the intensity is at quite high energies. To show this component more clearly, the antiferromagnetic scattering modeled as outlined above, has been subtracted. The residual scattering is plotted as a function of wave vector along the chain $Q_{\parallel}$. The feature at about 42 meV broadens and moves to lower vlaues of $Q_{\parallel}$ with increasing temperature. Now at low energies, and wave vectors sufficiently close to $Q_{\parallel}=2\pi/c$ one would expect the scattering to be described by a first-order field theory. This predicts a well-defined peak, which does not change with temperature, as shown by the solid line. However, the introduction of higher-order terms, Eq. (A8), leads to a broadened component. The dashed line shows the behavior of the second-order component alone. Although the data is not suitable for a quantitative comparison, consideration of these higher-order terms gives at least a qualitative description of the main features of the data.

The last figure of this paper is Fig. 17. This shows the high-energy response at temperatures of (a) 20, (b) 100 and (c) 150 K. The scattering profile calculated with the MA describes the high-energy response very well at every temperature. This is perhaps not surprising in that the energy transfers involved are considerably higher than the thermal energies. It is perhaps of interest to note that the boundaries of the scattering continuum appear to remain well defined at such temperatures.

V. SUMMARY AND CONCLUSION

In this paper the magnetic response for the 1D AF NNHM compound $KCuF_3$ has been studied in some detail using

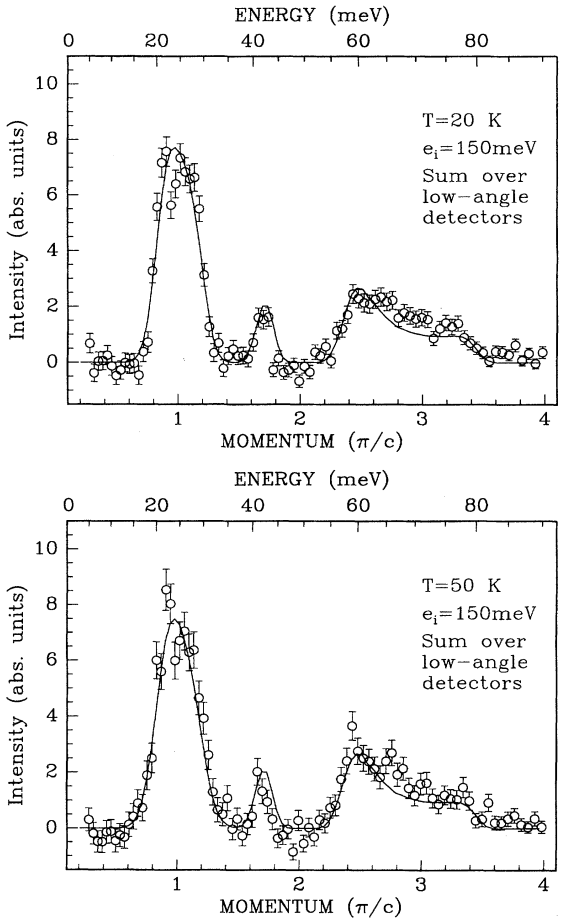

FIG. 14. Comparing the magnetic scattering in the low-angle banks for an incident energy of 148.9 meV. Top, below T_N, and bottom, above T_N.

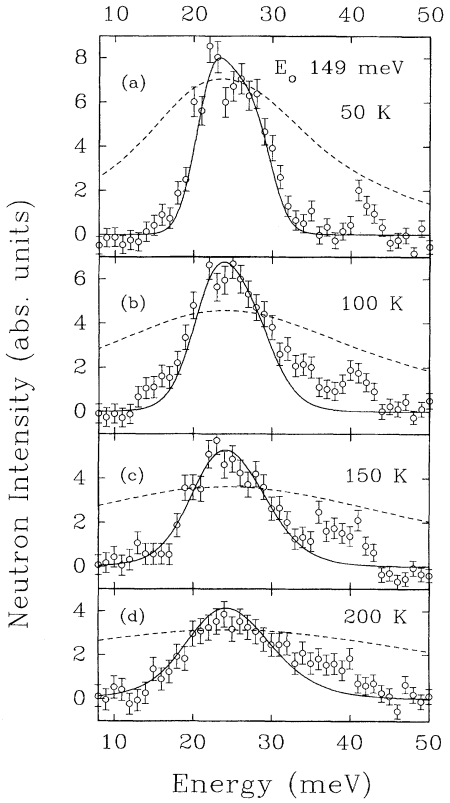

FIG. 15. Temperature dependence of the low-energy response. Measurements represent a summation over the low-angle detector banks. The nonmagnetic background for each scan has been determined and then subtracted. The measurements were all made with $\mathbf{k}_i \| c^*$ and using an incident energy of 148.9 meV. The solid line is a calculation using a quantum field theory (see text).

time-of-flight neutron scattering. Measurements made above and below the Néel temperature show strong quantum fluctuations. The magnetic response at $T=20$ K was probed using a number of different incident neutron energies. Normalization to a V standard allowed the absolute intensity of the scattering to be established with an uncertainty of $\pm 30\%$. The MA gives an excellent description of the data at low energies. Very little change was observed in the scattering cross section for measurements made at 50 K. Measurements at higher temperatures showed a broadening of the profiles at low-energy transfers. The field-theory calculations are in good agreement with the behaviour of the antiferromagnetic correlations at low energies. Broadening and renormalization of the excitations at higher energies are qualitatively understood by appealing to higher-order terms in the field operators.

ACKNOWLEDGMENTS

We are grateful to Dr. T. Perring and Z. Bowden for their assistance with the experiments and also to Dr. H. J. Schulz and Dr. I. Affleck for helpful discussions. Financial support was provided by the SERC (to whom D.A.T. is grateful for funding), and by the U.S. DOE under Grant No. DE-FG-05-92ER45280.

APPENDIX

The techniques of quantum field theory provide a general framework for calculating the physical properties of the $S=\frac{1}{2}$ AF NNHM. The method is to approximate the lattice of spins by a continuous field and then calculate the physical behavior on the basis of this field. This means that the predictions of such calculations are only valid at long wavelengths. For a one-dimensional system, the procedure of Luther and Peschel is usually followed. This maps the problem onto a new field φ with the following Hamiltonian:

$$H=\int dx\left(\frac{\pi}{2}\right)^2+v^2(\partial_x\varphi)^2, \tag{A1}$$

where π is the conjugate momentum field, and Bose commutation relations, $[\pi(x),\varphi(y)]=i\delta(x-y)$, are obeyed.

Our interest is in the spin-spin correlation functions predicted by field theory. To this end it is most convenient to work with the azimuthal magnetization density operator $m^z(x,t)$ defined by

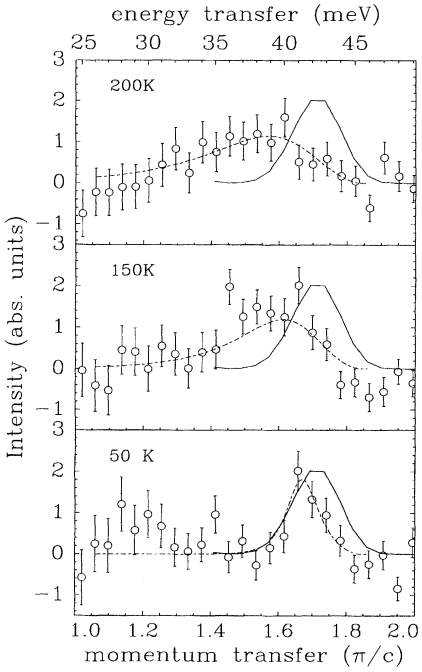

FIG. 16. The temperature development of the scattering near $Q=2\pi$. The solid line represents the first-order component, and the dashed line shows the second-order component (see text).

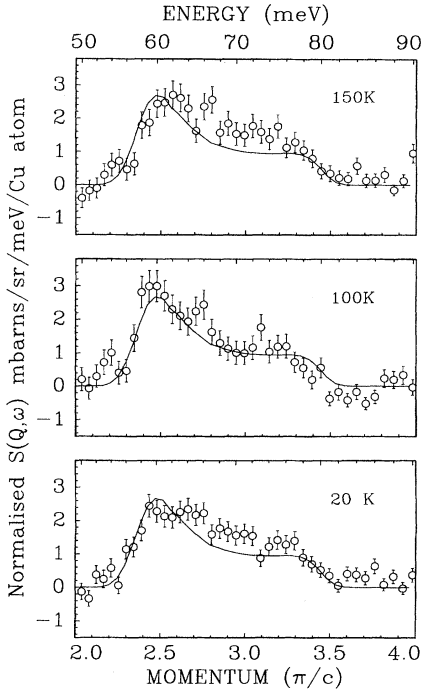

FIG. 17. The temperature development of the scattering at energy transfers above 50 meV. The background components have been subtracted, and the solid line is a calculation using the Müller form (see text).

$$m^z(x,t)=\frac{S^z_{2i}+S^z_{2i+1}}{2}=\frac{i\nu}{\sqrt{\pi}}\partial_x\varphi(x,t), \tag{A2}$$

which is a slowly varying function of x and t, and the staggered magnetization operator $a^z(x,t)$, defined by

$$a^z(x,t)=\frac{S^z_{2i}-S^z_{2i+1}}{2}\approx\lambda\ \cos(\varphi\sqrt{2\pi}). \tag{A3}$$

A constant λ has also been introduced; this has to be evaluated using other methods. Within the field representation, the spin operators are expressed as combinations of derivatives of the φ field and exponents. Only the operator expressions with the lowest scaling dimension have been retained on the right-hand side of Eqs. (A2) and (A3).

Because the x, y, and z components of spin are equivalent, only the correlations involving the z component of spin S^z need to be considered. The spin component S^z, in terms of a^z and m^z, is given by

$$\begin{aligned}S^z(x,t)&=m^z(x,t)+(-1)^n a^z(x,t)\\&=\frac{i\nu}{\sqrt{\pi}}\partial_x\varphi(x,t)+(-1)^n\lambda\ \cos[\varphi(x,t)\sqrt{2\pi}].\end{aligned} \tag{A4}$$

The correlation functions for the spin operators are interpreted as an order expansion in the field operators. To first order the Green's function for the azimuthal magnetization m^z is given by

$$\begin{aligned}G_m{}^{zz}(\mathbf{Q},\omega)&=-i\int_{-i\infty}^{+\infty}dt\ e^{i\omega t}\Theta(t)\langle[m^z_Q(t),m^z_{-Q}]\rangle\\&=\frac{1}{\pi}\frac{\nu Q^2}{\omega^2-Q^2\nu^2},\end{aligned} \tag{A5}$$

and the imaginary part of the Green's function is

$$\mathcal{I}G_m{}^{zz}(\mathbf{Q},\omega)=|Q|\,\delta(\omega-\nu|Q|), \tag{A6}$$

which gives a branch in $S(\mathbf{Q},\omega)$ with a structure factor of $|Q|$, emanating from the $Q=0$ point. This is in agreement with the MA, Eq. (4). The Green's function for the azimuthal magnetization does not change with temperature, and the only temperature-dependent factor in the scattering function is the detailed balance factor $(n_\omega+1)$. Similarly, the correlation functions for the staggered magnetization operator a^z can be found. This is given by

$$\begin{aligned}G_a{}^{zz}(\mathbf{Q},\omega)&=-i\int_{-\infty}^{+\infty}dt\ e^{i\omega t}\Theta(t)\langle[a^z_Q(t),a^z_{-Q}]\rangle\\&=\frac{1}{T}\rho\left(\frac{\omega-\nu Q}{4\pi K_B T}\right)\rho\left(\frac{\omega-\nu Q}{4\pi K_B T}\right),\\\rho(x)&=\frac{\Gamma(1/4-ix)}{\Gamma(3/4-ix)},\end{aligned} \tag{A7}$$

which is similar to Eq. (11), although the scattering emanates from $Q=0$ rather than $Q=\pi$.

The approximation to S^z given in Eq. (A4) can be modified, if necessary, by inclusion of terms with higher scaling

dimensions. The method by which this can be done is as follows: The total magnetization along the chain $S^T=\int S^z(x,t)dx$ is a conserved quantity of the motion; therefore the corresponding density must be a total derivative of some operator,

$$\hat{S}^z=\partial_x\hat{O}_1+(-1)^n\hat{O}_2. \tag{A8}$$

The operator with the smallest scaling dimension is $O_1\sim\varphi$ and the next one is $\sin(\sqrt{(2\pi)}\varphi)$, so

$$\partial_x\hat{O}_1=\frac{iv}{\sqrt{\pi}}\partial_x\hat{\varphi}+B\partial_x\cos(\sqrt{2\pi}\hat{\varphi}), \tag{A9}$$

where B is another undetermined constant reflecting the strength of the next-order term. Using this, the modified correlation function of the azimuthal magnetization is

$$G_m{}^{zz}(\mathbf{Q},\omega)=\frac{1}{\pi}\frac{v^2Q^2}{\omega^2-v^2Q^2}+CQ^2G_a{}^{zz}(\mathbf{Q},\omega)+\cdots, \tag{A10}$$

where C is an undetermined constant related to B in Eq. (A9). The spin-correlation function can be written in terms of Eqs. (A10) and (A3),

$$G_s{}^{zz}(\mathbf{Q},\omega)=-i\int_{-\infty}^{\infty}dt\ \Theta(t)e^{i\omega t}\langle[S^z_Q(t),\ S^z_{-Q}]\rangle$$
$$=G_m{}^{zz}(\mathbf{Q},\omega)+G_a^{zz}(|\pi-Q|,\omega). \tag{A11}$$

The last term on the right-hand side gives the scattering around the antiferromagnetic point, and, when multiplied by the detailed balance factor $(n_\omega+1)$, is proportional to the neutron-scattering cross section. The second-order term in Eq. (A10) provides an incoherent background to the ferromagnetic peak in the structure factor near $Q=0,2\pi$ and becomes progressively more important at higher energies and temperatures.

[1] I. Affleck, J. Phys. Condens. Matter **1**, 3047 (1989).
[2] H-J. Mikeska and M. Steiner, Adv. Phys. **40**, 191 (1991).
[3] F. D. M. Haldane, Phys. Rev. Lett. **50**, 1153 (1983); Phys. Lett **93A**, 464 (1983).
[4] See, for example, M. Steiner, J. Appl. Phys. **67**, 5593 (1990); J. P. Renard, J. Magn. Magn. Mater. **90**, 213 (1990), and references therein.
[5] S. E. Nagler, D. A. Tennant, R. A. Cowley, T. G. Perring, and S. K. Satija, Phys. Rev. B **44**, 12 361 (1991).
[6] K. Hirakawa and Y. Kurogi, Prog. Theor. Phys. S **46**, 147 (1970).
[7] G. Müller, H. Thomas, H. Beck, and J. C. Bonner, Phys. Rev. B **24**, 1429 (1981).
[8] H. J. Schulz, Phys. Rev. B **34**, 6372 (1986).
[9] H. A. Bethe, Z. Phys. **71**, 205 (1931).
[10] L. Hulthén, Ark. Mater. Astron. Fys. **26A**, 1 (1938).
[11] J. des Cloizeaux and J. J. Pearson, Phys. Rev. **128**, 2131 (1962).
[12] L. D. Faddeev and L. A. Takhtajan, Phys. Lett. **85A**, 375 (1981).
[13] M. Fowler, Phys. Rev. B **18**, 421 (1978).
[14] See, for example, S. W. Lovesey, *Theory of Neutron Scattering from Condensed Matter* (Clarendon, Oxford, England, 1987) or G. L. Squires, *Introduction to the Theory of Thermal Neutron Scattering* (Cambridge University Press, Cambridge, England, in press).
[15] P. C. Hohenberg and W. F. Brinkmann, Phys. Rev. B **10**, 128 (1974).
[16] V. S. Viswanath, *et al.* Phys. Rev. B **49**, 9702 (1994).
[17] F. D. M. Haldane, Phys. Rev. Lett. **60**, 635 (1988); **60**, 1866(E) (1988).
[18] B. S. Shastry, Phys. Rev. Lett. **60**, 639 (1988).
[19] F. D. M. Haldane and M. R. Zirnbauer, Phys. Rev. Lett. **71**, 4055 (1993).
[20] J. C. Talstra and F. D. M. Haldane (unpublished).
[21] E. Fradkin, *Field Theories of Condensed Matter Systems* (Addison-Wesley, Redwood City, CA, 1991).
[22] A. Luther and I. Peschel, Phys. Rev. B **9**, 2911 (1974); **12**, 3908 (1975).
[23] S. K. Satija, J. D. Axe, G. Shirane, H. Yoshizawa, and K. Hirakawa, Phys. Rev. B **21**, 2001 (1980).
[24] *User Guide to Experimental Facilities at ISIS*, edited by B. Boland and S. Whapham, RAL 92-041 (Rutherford Appleton Laboratory, England, 1992).
[25] J-C Li, D. Londono, D. K. Ross, J. L. Finney, S. M. Bennington, and A. D. Taylor, J. Phys. Condens. Matter **4**, 2109 (1992).
[26] P. J. Brown, in *International Tables for Crystallography*, Volume C, edited by A. J. Wilson (Kluwer Academic, Norwell, MA, 1992).